MARTIAN SURFACE TEMPERATURES

D. MORRISON

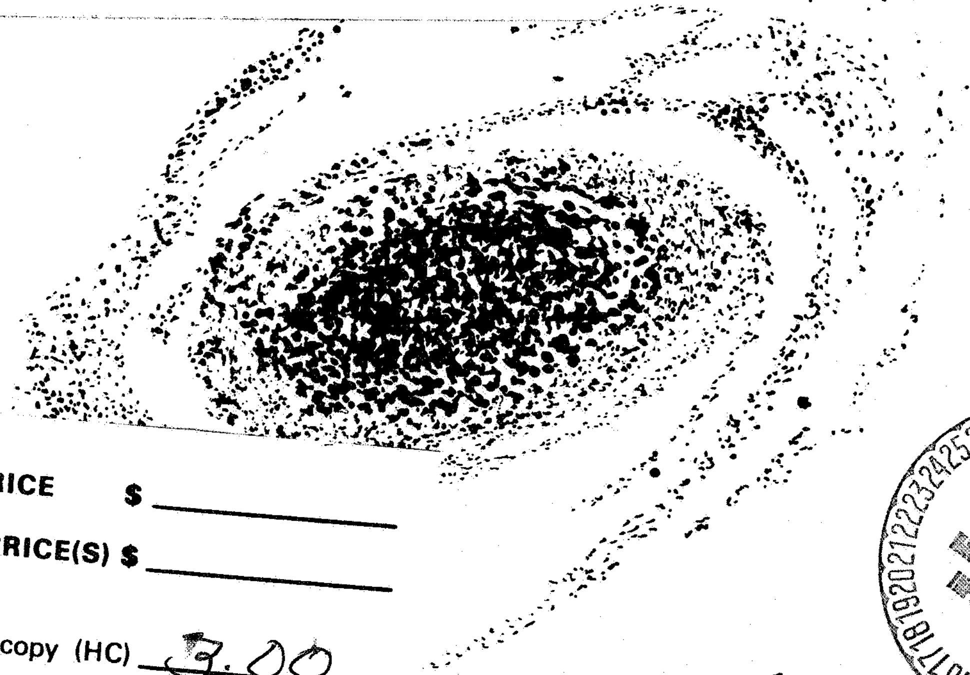

Smithsonian Astrophysical Observatory

SPECIAL REPORT 284

Research in Space Science
SAO Special Report No. 284

MARTIAN SURFACE TEMPERATURES

David Morrison

August 15, 1968

Smithsonian Institution
Astrophysical Observatory
Cambridge, Massachusetts 02138

807-10

TABLE OF CONTENTS

LIST OF ILLUSTRATIONS

LIST OF TABLES

ABSTRACT

The 8- to 13-μ thermal scans made of Mars in 1954 by Sinton and Strong are the best source of information available on the distribution of temperature over the disk. I have analyzed all these scans, normalizing to the center-of-disk temperature in the light areas of 290°K found by Sinton and Strong.

The observed equatorial temperature distribution between sunrise and midafternoon can be reproduced by a solution of the standard heat-conduction equation for a homogeneous subsurface when current values for the planetary albedo and emissivity are employed. The temperature range in the bright areas is from 303 to 180°K with a thermal inertia of 0.004 to 0.005 cal $cm^{-2} sec^{-1/2} deg^{-1}$; the thermal inertia of the dark areas is slightly larger. Mean particle sizes for the two areas are estimated from the thermal conductivities to be 20 to 40 μ and 100 to 300 μ, respectively.

The latitudinal temperature gradient is in accord with the above model for northern latitudes, but in the south the temperatures are depressed, consistent with the presence of a polar cap of frozen carbon dioxide. At all latitudes, a major fraction of the atmospheric water vapor is expected to condense at night. The radio brightness temperatures observed at centimeter wavelengths are also consistent with these thermal properties.

RÉSUMÉ

Les balayages thermiques de Mars entre 8 et 13μ qui ont été faits en 1954 par Sinton et Strong sont la meilleure source d'information utilisable concernant la distribution de température sur le disque. J'ai analysé tous ces balayages, en normalisant à la température du centre du disque de 290°K trouvée par Sinton et Strong dans les régions claires.

La distribution de la température équatoriale observée entre le lever du soleil et le milieu de l'après-midi peut être reproduite par une solution de l'équation classique de la conduction thermique d'une sous-surface homogène, quand des valeurs courantes de l'albedo et de l'émissivité planétaires sont employées. La gamme de température dans les régions claires s'étend de 303 à 180°K avec une inertie thermique de 0,004 à 0,005 cal cm^{-2} $sec^{-1/2}deg^{-1}$; l'inertie thermique des régions sombres est légèrement plus grande. Les tailles des particules moyennes sont estimées à partir des conductibilités thermiques à être respectivement de 20 à 40μ et de 100 à 300μ pour les deux régions.

Le gradient de température latitudinale est en accord avec le modèle ci-dessus pour les latitudes du Nord, mais au Sud les températures sont abaissées, ce qui est compatible avec la présence d'une calotte polaire de carbone dioxide gelé. On présume qu'une importante fraction de la vapeur d'eau atmosphérique se condense la nuit à toutes les latitudes. Les températures de brillance observées aux ondes centimétriques sont aussi compatibles avec ces propriétés thermiques.

КОНСПЕКТ

Наилучший источник доступных сведений о распределении температуры по диску является 8 до 13μ термическое изображение Марса полученное Синтоном и Стронгом в 1954 году. Я проанализировал все эти изображения, нормализируя их по температуре в центре диска в светлых областях в 290° К полученных Синтоном и Стронгом.

Распределение экваториальной температуры наблюдаемое между солнечным восходом и серединой после полудня могут быть воспроизведены путем решения стандартного уравнения теплопроводности для однородной подпочвы в случае когда употребляются настоящие величины для планетарной альбедо и излучательной способности. Температурный диапазон в ярких областях колеблется между 303 и 180° К с термической инерцией от 0,004 до 0,005 кал.$см^{-1}сек^{-1/2}$ $градус^{-1}$; термическая инерция темных областей немного больше. Средние размеры частиц для обоих областей исходя из теплопроводности были оценены между 20 и 40μ и 100 и 300μ соответственно.

Широтный температурный градиент согласуется с выше описанной моделью для северных широт, но на юге температуры пониженны последовательно с присуствием полярной шапки замороженного углекислого газа. Ожидается что наибольшая часть атмосферного водяного пара конденсируется по ночам. Температуры радио-яркости наблюдаемые на сантиметровых длинах волн также согласуются с этими термическими свойствами.

MARTIAN SURFACE TEMPERATURES

David Morrison

1. INTRODUCTION

Determination of the surface temperature of Mars and of its diurnal and seasonal variations has been a topic of scientific investigation for many decades. In their classic exchange at the beginning of this century, Lowell (1906) and Wallace (1907) both concluded that the maximum temperature was similar to that of the earth, since the greater distance of Mars from the sun was compensated for by its lower albedo. (At noon at the mean distance from the sun, the theoretical temperature, when atmosphere and subsurface heat conduction are neglected, varies from 320°K for a perfect blackbody to 298°K for an albedo of 0.25.) However, Wallace stressed that Mars, lacking the moderation of oceans or the greenhouse effect of a massive atmosphere, should experience rapid radiative cooling at night, leading to a low mean temperature and a large diurnal temperature range.*

In the 1920's, Coblentz and Lampland at Lowell Observatory and Pettit and Nicholson at Mount Wilson made the first measurements of Martian surface temperatures. From a reanalysis of the observations of Lampland, Gifford (1956) gives a peak temperature of 280°K, somewhat lower than expected. The temperature maximum also appeared to fall several hours after noon on the planet, indicative of a thermal conductivity much greater than that of the moon.

This research was supported in part by grant NGR 09-015-023 from the National Aeronautics and Space Administration.

*Wallace also made the interesting suggestions that the surface of Mars is covered with a dusty, porous layer of low thermal conductivity and that the temperatures are too low for the polar caps to melt at the observed rate if they are composed of ice. While he mentioned that temperatures might be low enough for carbon dioxide to freeze, he did not consider that the Martian polar caps might be carbon dioxide.

During the favorable Martian opposition of 1954, Sinton and Strong of Johns Hopkins University used the 200-inch telescope on Mount Palomar to make thermal maps of Mars with an angular resolution of 1.5 arcsec. They found an average temperature at the center of the disk of 292°K and made 33 scans across the planetary disk to determine the variation of temperature with position. From six of the equatorial scans, Sinton and Strong (1960a) derived a value for the thermal inertia of the surface of between 0.004 and 0.010 cal cm^{-2} $sec^{-1/2}$ deg^{-1} and estimated a nighttime minimum temperature of about 200°K.

The thermal observations of Sinton and Strong remain the best available, and several authors making theoretical studies of Mars have utilized them (Leovy, 1966; Leighton and Murray, 1966; Gierasch and Goody, 1968). The six published scans represent only a fraction, however, of the data obtained by Sinton and Strong. In this report, I discuss a new reduction of all the 1954 scans. From this larger body of data, it is possible to construct a temperature map of the daytime face of the planet and to refine the determination of the variation of equatorial temperature with solar hour angle. I also discuss the determination of the thermal properties of the planetary surface from these data and the implications of the results for the study of the meteorology of Mars and the mechanical properties of its surface material.

2. DATA REDUCTION

Sinton and Strong (1960a, b) have given detailed descriptions of their observational and data-reduction techniques. Briefly, the observations were made with an infrared radiometer at the coudé focus of the 200-inch telescope in July 1954. The detector was a Golay cell, exposed to radiation alternately from the planet and from the adjacent sky, with a chopping frequency of 10 Hz. The passband of the system was defined by the atmospheric window between 7 and 14 μ, with an Eastman Kodak silver sulfide filter used to exclude all wavelengths short of 5.5 μ. The entrance aperture was 1.5 arcsec, and the time constant of the system, 4 sec. The same instrument was also used with slight modification to measure the temperature of the center of the disk. In this mode of operation, a reflection from an uncoated quartz flat at 14° incidence was used to weight the sensitivity of the system toward 8.9 μ, where atmospheric transmission is relatively great, and the entrance aperture was increased to 5 arcsec. A comparison of the planetary flux with that of temperature-controlled blackbody cavities provided the calibration.

All the observations were made at zenith distances of between 63° and 72° during twilight before the regular observing program of the telescope began. Calibrations were made for the quartz-band observations used to determine the temperature near the center of the disk, but they were not made for the high-resolution scans. To reduce the six equatorial scans they published, Sinton and Strong normalized each to the same deflection at the disk center; they then converted them to temperature, using a plot of instrumental deflection as a function of the temperature they obtained from observations made in 1953 with a monochromator transmitting in a band from 8.2 to 12.4 μ. To confirm the applicability of their plot to these observations, I have computed the expected flux in the atmospherically limited instrumental band as a function of temperature for a blackbody radiator, using the atmospheric transmission given by Sinton and Strong (1960b). Figure 1 gives this computed flux as a function of the fourth power of the temperature; this is the form used by Sinton and Strong, although we could equally well plot against any power of the temperature. The instrumental deflection should be proportional to this flux.

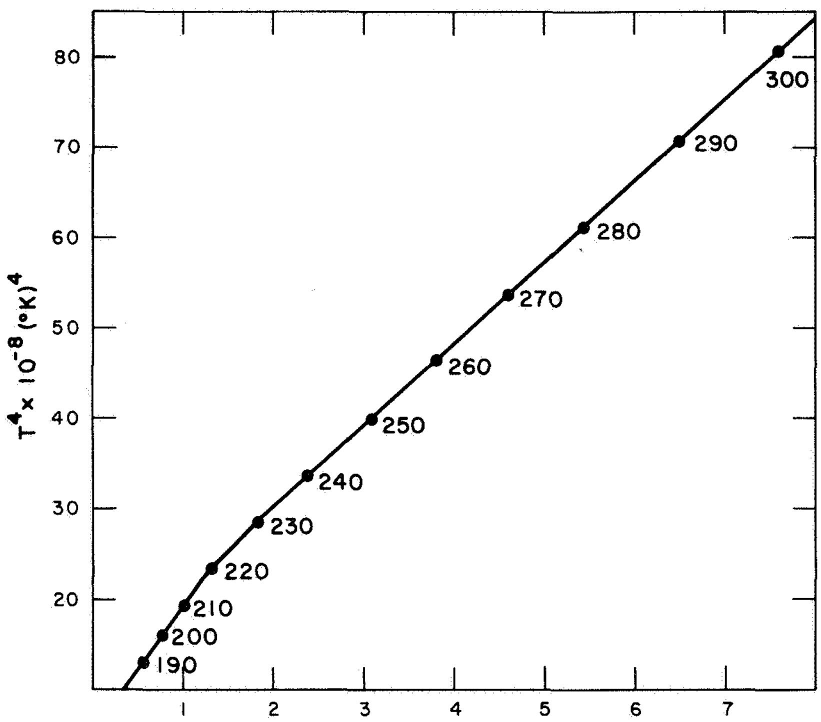

Figure 1. The abscissa is the response of the infrared radiometer, through the 8- to 13-μ atmospheric window, as a function of the fourth power of the temperature of the planet. The response scale is arbitrary. Temperatures given on the curve are in °K.

For each of the 33 scans of Mars, Sinton and Strong (1960c) have published a tracing of the deflection as a function of time and a corresponding plot of the path of the scan across the planetary disk. Figure 2, taken from their report, shows this information for three scans. The path across the disk was determined from photographs taken with a camera mounted behind the beam chopper of the instrument; the numbers in Figure 2 correspond to these measured positions. Between two and four such determinations were made during each scan.

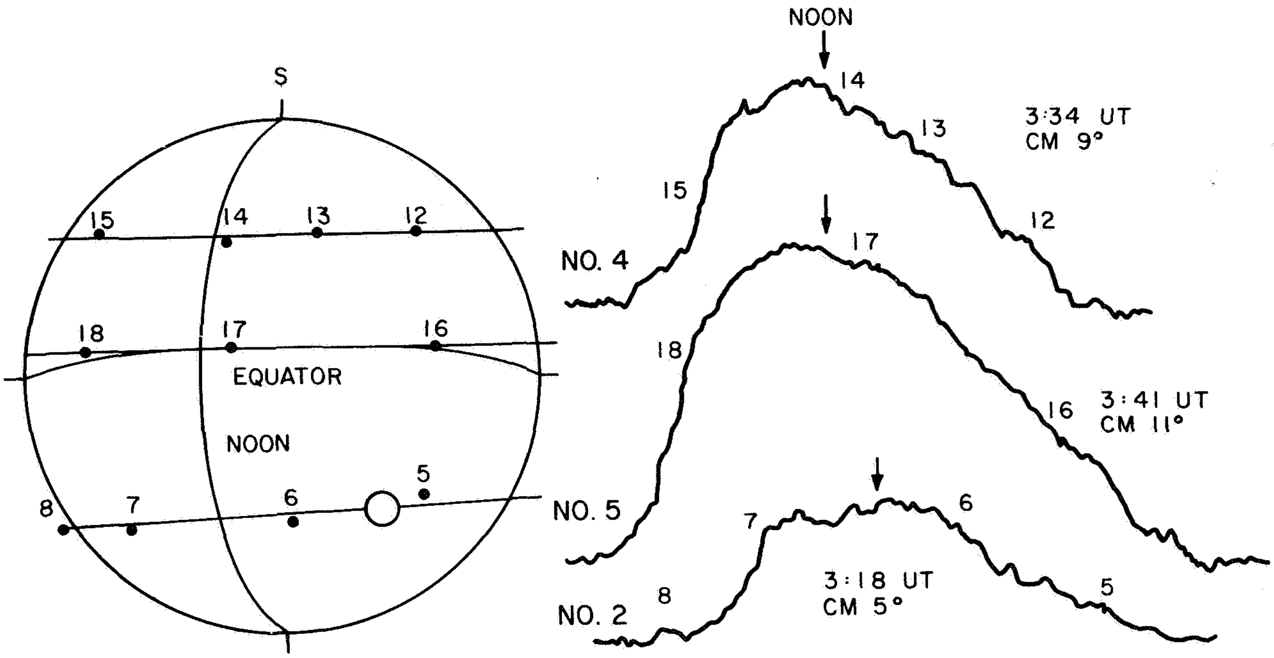

Figure 2. Analog records of Martian scans as presented by Sinton and Strong (1960a). The open circle illustrates the size of the 1.5-arcsec aperture.

To utilize the hundreds of individually measured temperatures that can be derived from these data, I have digitized the deflections and positions at intervals of 1 arcsec along each scan. The deflections were measured on an arbitrary scale above a base line that I drew, and the positions were expressed in a Cartesian (x, y) coordinate system centered on the disk, which was assumed to have unit radius with south at the top.

At the time of observation, Mars had a phase angle of 18° and the latitude of the subearth point was +5°; thus, a coordinate transformation that includes rotations is necessary for deriving planetary latitudes and longitudes from the (x, y) positions. These general transformation equations are derived in Appendix A. Using them, I found for each point the areographic latitude, longitude, and solar hour angle, and also the zenith distances of the sun and the earth. It should be noted that, near the limb, these are extremely sensitive to the (x, y) coordinates and hence to any errors in the photographically determined scan positions given by Sinton and Strong.

I first made a preliminary reduction of the data, based on the assumption that the same deflection scale applies to all the analog records. In this way the general variation of temperature across the disk was obtained. The peak temperature was found to be 10° to 12° higher than the temperature at the center of the disk determined by Sinton and Strong with the 5-arcsec aperture, and the variation of temperature with latitude for $|y| < 0.25$ was found to be less than 2°. With this information (confirmed in the final reduction), I reconverted the deflections to temperatures for all east-west scans with $|y| < 0.25$, using the relation of Figure 1 and normalizing each scan to 300°K at its peak. The resulting average run of temperature with x provided in turn the normalization for all the north-south scans. Finally, the nonequatorial east-west scans were normalized to the two standard north-south scans discussed below, although because of the repeated normalizations these east-west scans were given lower weight in the final reductions.

Figure 3 illustrates the paths across the disk of two particularly interesting sets of north-south scans. On July 20, scans 9 and 10 were made in quick succession crossing the equator at solar hour angle + 4° and passing over Sinus Meridiani. Scan 14 from that date and scans 3 and 8 from July 21 all crossed the equator at hour angle - 35° to - 40°; because of planetary rotation, however, only scan 8 crossed Sinus Margaritifer. The variation of temperature with y for these two sets of scans is shown in Figure 4; these are also the temperatures used to normalize the nonequatorial east-west scans. The temperature of Sinus Meridiani near noon is 5° to 6° higher than that of the surrounding light areas; it also appears that the temperature on Sinus Margaritifer is elevated by about 4°. In addition, there is evidence of a temperature elevation of comparable size on Syrtis Major. These values are all derived from north-south scans, since the diurnal variation of temperature with position is too great on east-west scans to permit differences between light and dark areas to be reliably determined. Sinus Meridiani,

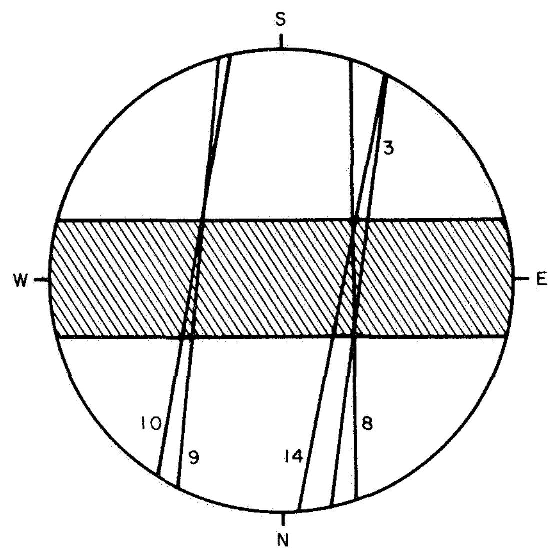

Figure 3. Paths of the north-south scans discussed in the text. The cross-hatched area is that used to compute the standard equatorial temperature variation to which the north-south scans were normalized.

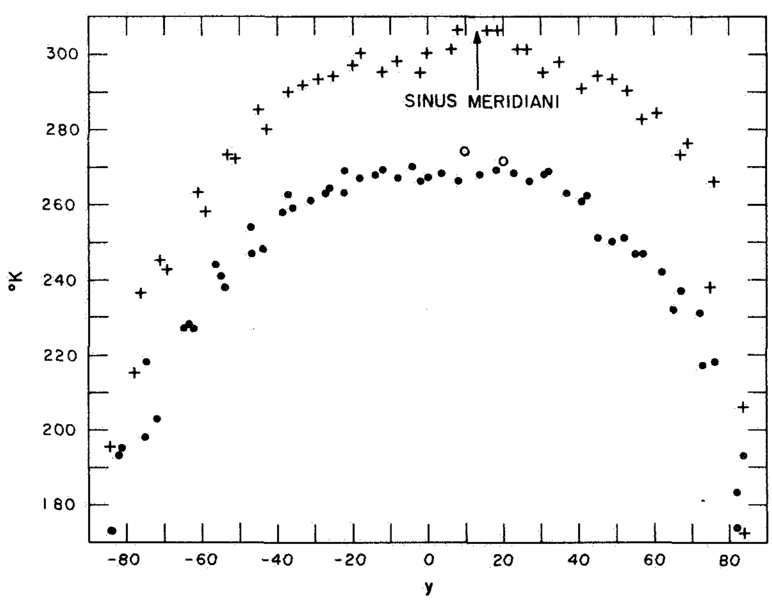

Figure 4. The two sets of north-south scans shown in Figure 3. The crosses are scans 9 and 10 from July 20; the circles are scan 14 from July 20 and scans 3 and 8 from July 21. The two open circles are measurements of Sinus Margaritifer.

Sinus Margaritifer, and Syrtis Major are the three major dark areas for which there are data; north-south scans crossing paler dark areas such as Sinus Sabaeus show no evidence of an elevated temperature. For this reason, I have treated all temperatures not lying in one of these three major dark areas as representative of the predominant light areas of the planet.

From the internal contradictions in the photographically determined positions indicated by Sinton and Strong for each scan, it appears that some scans may have large position errors. In three cases, I was able to correct these errors by noting the discontinuity in temperature where a scan appeared to pass near a prominent dark area and by shifting the scan to place the discontinuity at the correct areographic coordinates. In all such cases, the entire scan was shifted, so that no allowance was made for possible variation in the scan rate. Even after this adjustment, a number of nonzero temperature points remain for positions that should be off the disk, indicating that a typical error in position for a point may be 1 arcsec.

The reductions described above yield approximately 600 measured temperatures on the disk of Mars. These data are listed in Appendix B. I have grouped the data by regions, 10° by 10° in latitude and solar hour angle, and have computed an average temperature for each region. Excluding points measured in the major dark areas or in the position of the yellow cloud present on July 20, I have obtained the brightness temperature map of Mars shown in Figure 5. All points more than 65° from the subearth point (and hence within 1 arcsec of the edge of the disk) were omitted. Figure 6 shows the variation of brightness temperature with solar hour angle in the equatorial regions; all east-west scan data from light areas between latitude -20° and +10° were included. The error bars show the standard deviation in the mean for each point. These data are also listed in Table 1, to be discussed below.

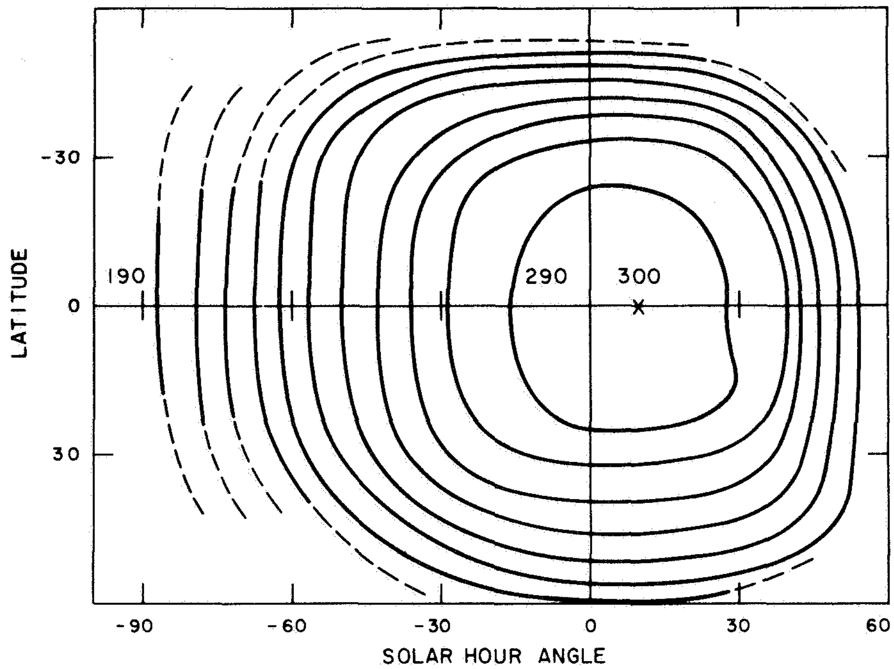

Figure 5. Brightness temperature map of Mars. All data from light areas are included. The dashed isotherms are known with less accuracy than the solid lines. Contour interval is 10 K°.

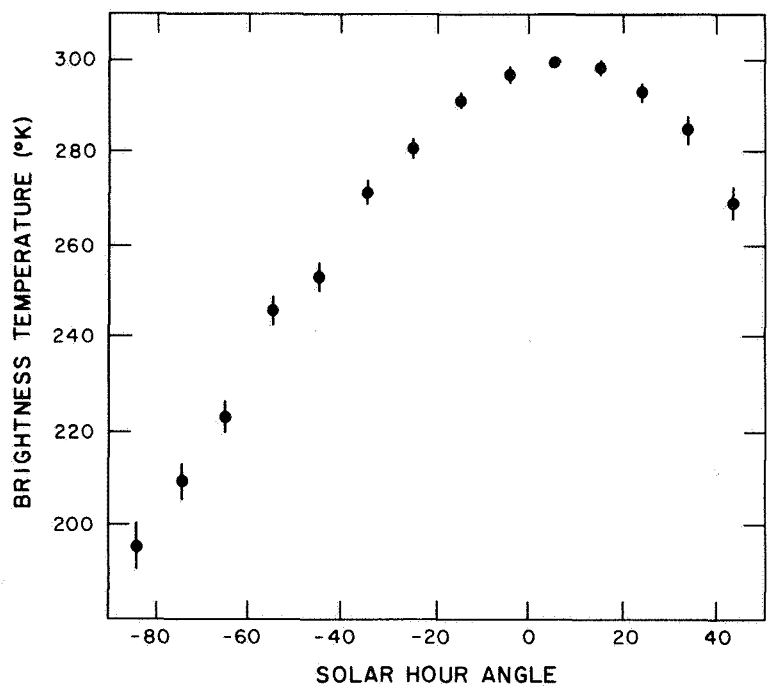

Figure 6. Variation of equatorial brightness temperature of Mars with solar hour angle. Error bars show standard deviation in the mean for each point.

In interpreting these temperatures on Mars, I have considered the problem of deducing a temperature from the nonlinear average made by the instrument, which measures thermal flux, over its field of view. As shown in Appendix C, the correction to the temperature should be less than 1% for these data, unless a large amount of seeing motion during the 4-sec integration period of the instrument caused the aperture to average over an area of the disk much more than 1.5 arcsec in diameter; if this was the case, all the limb temperatures given here are several degrees too high.

In many cases we wish to know the true thermometric temperatures as well as the brightness temperatures discussed above. To convert to thermometric temperature, we divide the brightness temperature by the nth root of the radiometric emissivity, where n is given by

$$n = \frac{1.439}{\lambda T}$$

(see Appendix C). For $\lambda = 10\ \mu$, n varies from 4.8 at 300°K to 8.0 at 180°K. I have used the infrared reflectance measurements between 0.5 and 22 μ made by Hovis and Callahan (1966) on crushed samples of terrestrial rock to estimate the radiometric emissivity for such materials. Taking the emissivity at each wavelength as 1 minus the observed reflectance, I weighted it by the Planck function for each choice of temperature and found the average over the spectrum. The resulting radiometric emissivities are found to be virtually independent of temperature in the range 200 to 300°K. Depending on particle size, the values lie between 0.89 and 0.96, independent of mineral composition, with 0.93 the preferred choice for particles less than 0.1 mm in size. A similar analysis gives a value of 0.95 for the emissivity in the 8- to 13-μ spectral band, independent of temperature, composition, or particle size.

If the 8- to 13-μ emissivity is isotropic, the factor needed to convert to thermometric temperature varies from 1.011 at 300°K to 1.005 at 180°K. If, however, the emissivity has a directional dependence like that found by Sinton (1962) for the moon, then near the limb a larger correction must be applied to convert the observations to thermometric temperatures. The equatorial temperature data are summarized in Table 1, where T_B are the brightness temperatures plotted in Figure 6, T_1 are the surface temperatures obtained by use of the isotropic emissivity, and T_2 are obtained with a lunar variation of emissivity with direction, normalized to a mean of 0.95. The final columns give the standard deviation σ_T in the temperature and the number of data points N that were averaged.

Table 1. Equatorial brightness temperatures and thermometric temperatures

Solar hour angle	T_B(°K)	T_1(°K)	T_2(°K)	σ_T(K°)	N
- 84	195	196	202	16	8
- 74	209	210	215	11	8
- 65	223	225	229	9	7
- 55	246	248	249	9	11
- 45	253	255	255	8	9
- 35	271	274	274	7	7
- 25	281	284	283	7	11
- 15	291	294	293	4	12
- 4	296	300	299	3	10
+ 5	300	303	303	1	9
+ 15	299	302	303	1	8
+ 24	293	296	298	1	6
+ 34	285	288	293	6	6
+ 43	269	272	280	8	7

3. COMPARISON WITH THERMAL MODELS

For a planet with little or no atmosphere, the surface and subsurface temperatures can be computed directly from a solution of the one-dimensional heat-conduction equation with appropriate radiative boundary conditions. Analytic solutions for the simple case of the moon have been obtained by Wesselink (1948) and Jaeger (1953) and have been applied to Mars at its equinox by Sinton and Strong (1960a). However, a numerical solution by digital computer is much more flexible, especially when the insolation departs from a simple sine wave (see, e.g., Linsky, 1966; Leighton and Murray, 1966; Morrison and Sagan, 1967). For this report, I have obtained computer solutions to the heat-conduction equation for a homogeneous, plane-parallel medium with thermal properties independent of depth and temperature. The computer is capable of reproducing the diurnal insolation for any season and for any position on Mars. I have not considered the effects of the latent heat of volatiles, since carbon dioxide will not condense at temperatures appropriate to equatorial and temperate latitudes (Leighton and Murray, 1966), while water, which will condense, is present in quantities so small as to have a negligible influence on the temperature.

Sinton and Strong (1960a) and Leovy (1966) have suggested that the atmosphere on Mars may play an important role in the determination of surface temperatures. However, it is now known that the atmosphere is much less massive than had been supposed, and recent calculations by Gierasch and Goody (1968) have indicated that the atmosphere has very little effect on surface temperatures. There is a small radiative flux downward that is nearly independent of time and has a magnitude of about 1% of the noon solar flux (P. Gierasch, 1967, private communication). I have included this greenhouse effect in my calculations, where it serves to increase the night temperatures by a few degrees; the corresponding increase in the mean daily temperature is somewhat smaller than the value of 8°5 suggested for this quantity by Sagan and Pollack (1968). I have neglected all other atmospheric effects and have computed temperatures to be compared with the observations by a straightforward solution of the heat-conduction equation.

The three parameters that must be specified for each model are the bolometric albedo, the radiometric emissivity, and the thermal inertia $(K\rho c)^{1/2}$ cal cm^{-2} sec$^{-1/2}$ deg^{-1}, where K is the thermal conductivity, ρ is the density, and c is the heat capacity of the subsurface material. As discussed above, I find from the data of Hovis and Callahan (1966) that an appropriate radiometric emissivity is 0.93. The bolometric albedo is given by de Vaucouleurs (1964) as 0.30 ± 0.02 (p. e.), while Walker (1966) finds from his measurements of the albedo in the infrared that the value should be 0.23. The above apply to the planet as a whole. The differential colorimetry of McCord (1968) compares the brightness of light and dark areas; he finds that the dark areas have half the albedo of the bright areas near 1-μ wavelength, while the contrast decreases to shorter wavelengths until it is negligible short of 4500 Å. It therefore seems likely that the bolometric albedo of the bright areas is near 0.25 and that of the dark areas is somewhat more than half this amount. Figure 7 shows the variation of peak surface temperature as a function of albedo and thermal inertia computed for the subsolar latitude on Mars on July 20, 1954, with an assumed emissivity of 0.93. At the average distance of Mars from the sun, these temperatures would be about 10° lower. Adopting an albedo of 0.25 for the bright areas, we see that the observed peak temperature of 303°K (Table 1) indicates a thermal inertia of between 0.004 and 0.005 cal cm^{-2} sec$^{-1/2}$ deg^{-1}; for dark areas of albedo 0.15 and peak temperature 308°K, the thermal inertia is 0.006 cal cm^{-2} sec$^{-1/2}$ deg^{-1}. In order for the light and the dark areas to have the same thermal inertia, their peak temperatures would have to differ by 10° for this choice of albedo; alternatively, the thermal inertias could be the same for a 5° temperature difference if the albedos were 0.25 and 0.20, respectively.

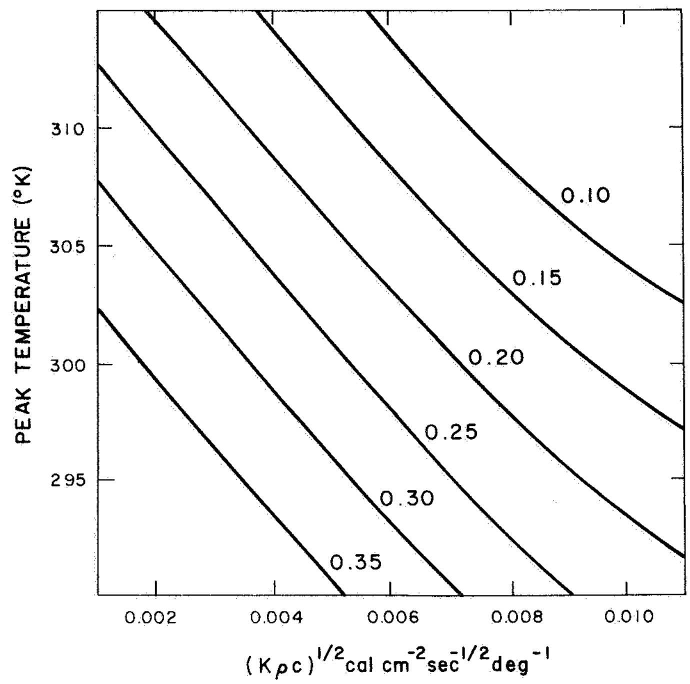

Figure 7. Peak thermometric surface temperature on Mars as a function of thermal inertia $(K\rho c)^{1/2}$ for a number of bolometric albedos. Computations are made for latitude - 8° and heliocentric longitude 290°. The radiometric emissivity was taken to be 0.93.

Figure 8 compares the equatorial temperatures with those predicted by the heat-conduction calculations for an albedo of 0.25 and two choices of thermal inertia. Both temperatures T_1 and T_2 of Table 1 are plotted. As indicated above, a thermal inertia of 0.004 cal cm^{-2} $sec^{-1/2}$ deg^{-1} fits very well near the peak; the fit is also acceptable over the rest of the curve, although the 0.006 thermal-inertia curve fits equally well in most places. The only serious problems arise for the point at solar hour angle +43°; here, the fit is significantly better if we use the emissivity that varies with direction. This point may also be too low because of the presence of a cloud near the afternoon limb; it is known (Sinton and Strong, 1960a) that such a cloud was present nearby on July 20. This low point is, of course, little more than 1 arcsec from the limb of the planet. On the whole, the fit of these two computed curves to the data seems very satisfactory, and the values for the thermal inertia of 0.010 suggested by Sinton and Strong (1960a) and of 0.002 deduced by Leovy (1966) can probably be excluded.

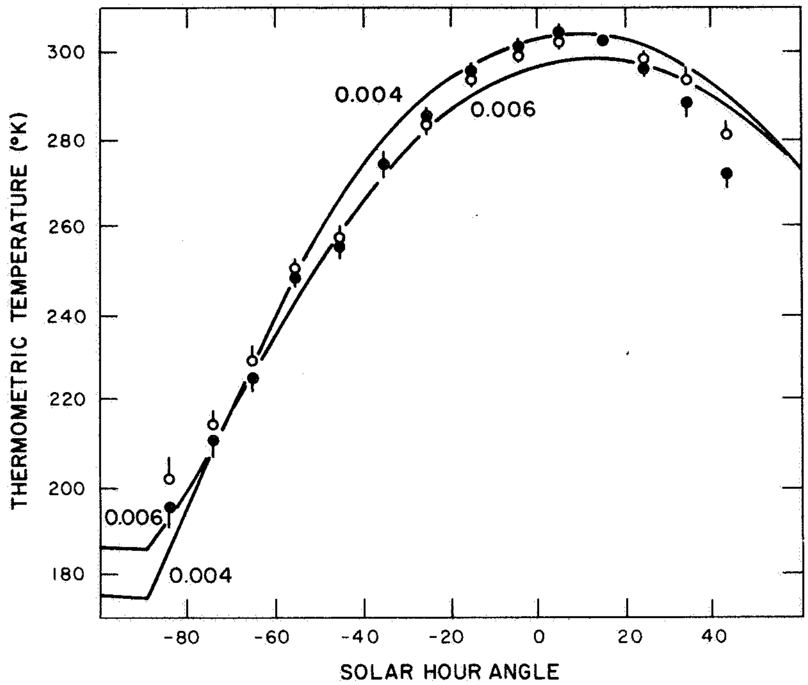

Figure 8. Comparison of the data with theoretical curves obtained from heat-conduction models. Filled circles are T_1, and open circles are T_2 (see Table 1). Only half of each error bar (representing the standard deviation in the mean) is shown. The theoretical curves are labeled by the assumed thermal inertia $(K\rho c)^{1/2}$ cal cm^{-2} $sec^{-1/2}$ deg^{-1}.

I have computed the expected distribution of temperature for the light and the dark areas on Mars at the equinox (heliocentric longitude = 268°) using the combinations of thermal inertia and albedo suggested above; the results are shown in Figure 9. The dark areas are always hotter than the light, although during midmorning this difference is very small. The greatest temperature differences, about 15°, develop near sunset and persist throughout the night. If such temperature differences do exist on Mars between adjacent light and dark areas, they may drive winds that are analogous to the terrestrial sea breeze.

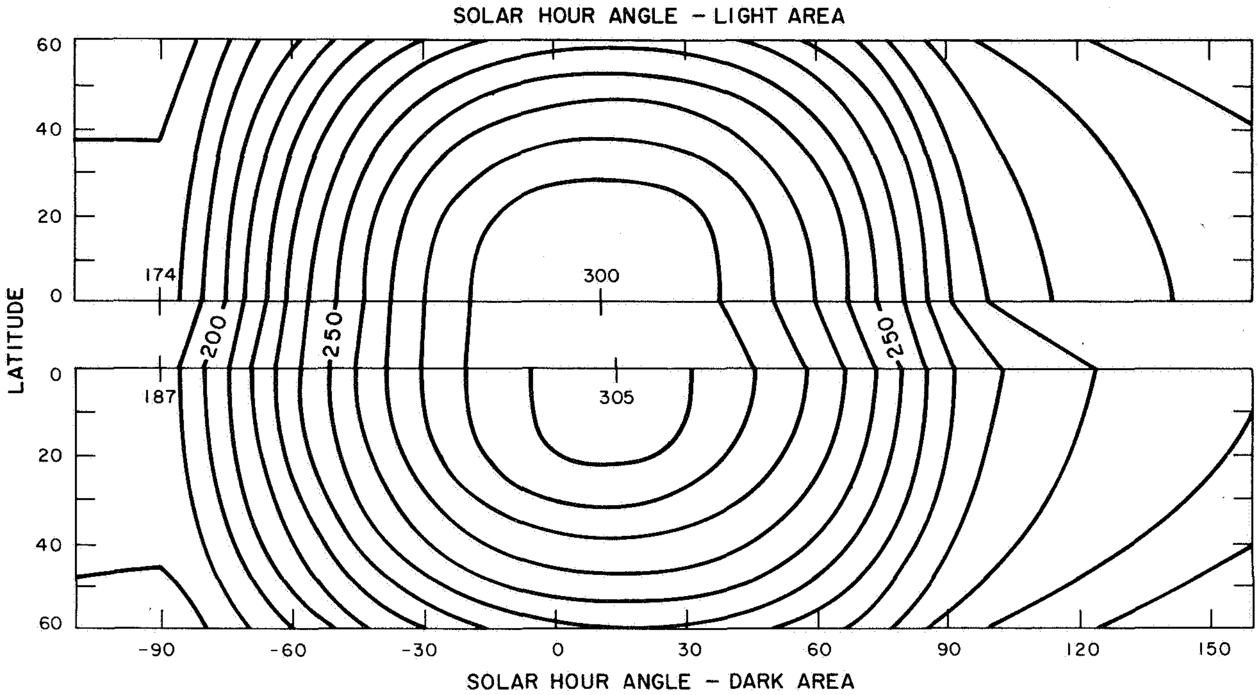

Figure 9. Theoretical temperature distribution with latitude and solar hour angle for Mars at the equinox (heliocentric longitude = 268°). The upper map was computed for light areas: albedo = 0.25 and thermal inertia = 0.004 cal cm^{-2} $sec^{-1/2}$ deg^{-1}. The lower map represents dark areas: albedo = 0.15 and thermal inertia = 0.006 cal cm^{-2} $sec^{-1/2}$ deg^{-1}.

Using data from north-south scans only, I have found the average variation of brightness temperature with latitude in the three regions of solar hour angle shown in Figure 10. The curve in this figure is the thermometric temperature expected from the model with thermal inertia 0.004 and albedo 0.25 at heliocentric longitude 290°. When allowance is made for the difference between brightness temperature and thermometric temperature, we see that in the Northern Hemisphere the data fit the curve very well. In the Southern Hemisphere, however, the data show a more rapid temperature drop than at the corresponding positive latitudes, while the theoretical curves drop more slowly. This difference is due to seasonal effects that were not allowed for in the computation of theoretical curves; it was spring in the Southern Hemisphere at the time of the observations, and the ground was cooler than would be expected from insolation alone. In addition, there was still a large south polar cap. If the cap shrank in 1954 at the same rate as observed in 1924 (Slipher, 1962), its edge should have been near latitude -60°. A linear extrapolation from Figure 10 indicates that the temperature at this latitude was probably below 160° and is entirely compatible with a polar cap of frozen carbon dioxide at a temperature of 145°K, as suggested by Leighton and Murray (1966) and Gierasch and Goody (1968).

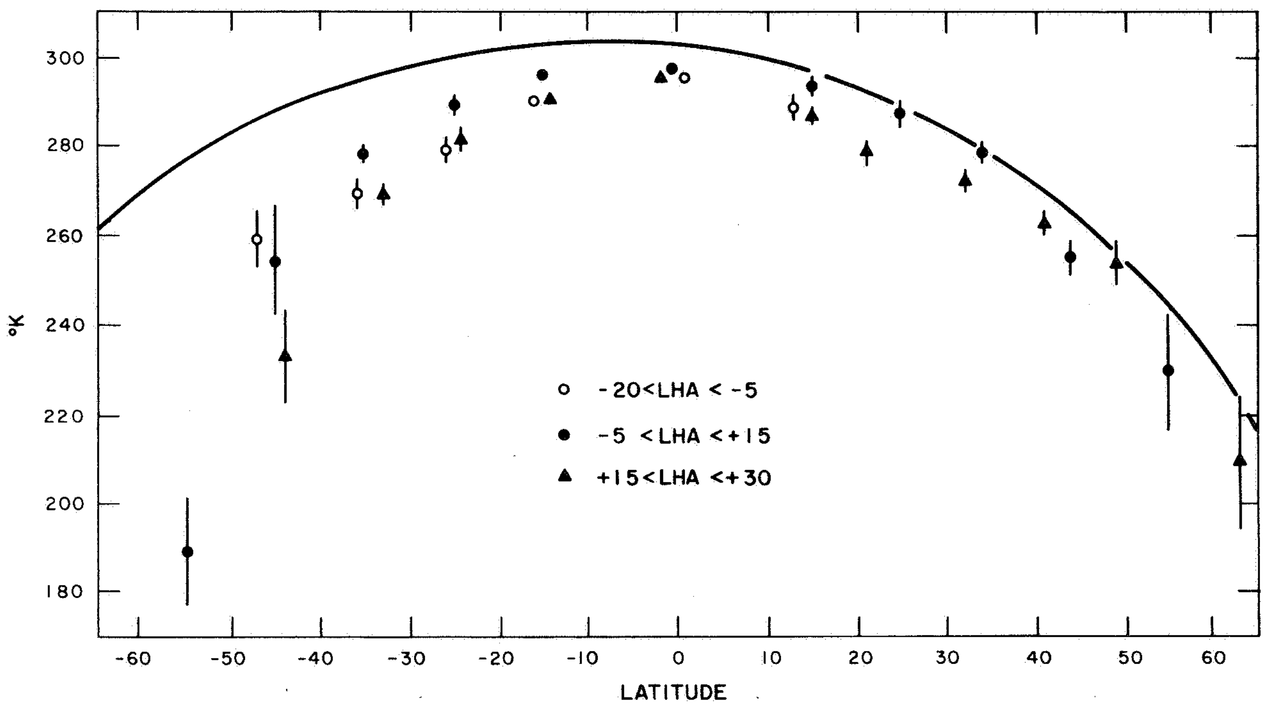

Figure 10. Variation of temperature with latitude. The data points are average brightness temperatures with indicated standard deviations in the mean. The solid curve is the theoretical peak thermometric temperature for an albedo of 0.25 and a thermal inertia of 0.004 cal cm^{-2} $sec^{-1/2}$ deg^{-1}.

For the two thermal models of Figure 9, I have computed the disk temperature (assuming unit emissivity) that would be observed at radio wavelengths of a few centimeters. The flux was averaged over the disk by means of techniques developed for the planet Mercury (Morrison and Sagan, 1967); the temperature distribution in the two hemispheres was assumed to be identical, and no allowance was made for seasonal effects. The resulting disk temperature for the bright areas is 220°, and that for the dark areas, 228°K; reduced to the mean distance of the planet from the sun, these temperatures become 215 and 223° K. These numbers have probable errors of less than 5°, and their relative error is less than 2°. The radar reflectivity of Mars at a wavelength of 12.5 cm is about 8% (Goldstein, 1965); applying an emissivity of 0.90 to the above temperatures* gives disk brightness temperatures of 193 and 201°K, respectively. The brightness temperature observed at 3.75 cm by Dent, Klein, and Aller (1965), reduced to mean distance from the sun, is 190° ± 12°K, in good agreement with the computed number for the predominant bright areas of Mars. The requirement that a thermal model reproduce the observed high surface temperatures at noon and still predict a mean radio brightness temperature as low as 200°K effectively excludes values of the thermal inertia as high as 0.010 cal cm^{-2} $sec^{-1/2}$ deg^{-1}. The radio brightness temperature offers an especially powerful argument for low nighttime surface temperatures on Mars, since the conclusions do not depend on the assumed model of homogeneous subsurface heat conduction with negligible moderation by the atmosphere.

The preceding discussions have dealt only with models that specify a single value of the thermal inertia for the epilith.† It is quite reasonable, however, to imagine that, on a scale that is small with respect to the area observed by the aperture, there is a mixture of components (such as sand and rocks) having different thermal properties. I have experimented with combining the fluxes in various proportions from two thermal models to obtain average temperatures to be compared with the observations. The temperature curves from most such two-component models differ very little from those generated with a single component. For instance, the curves of Figure 8 can be closely duplicated by combining fluxes from 60 to 80% material with

---

*The determination of microwave emissivity from radar cross section depends on the model assumed for the surface (see Rea, Hetherington, and Mifflin, 1964); the number 0.90 is only approximate.

†This term for the particulate upper layer of a planet is recommended by Johnson (1968).

a thermal inertia of 0.002 with those from 20 to 40% material with inertias of 0.010 or greater. While such combinations are not excluded by the data, neither are they an improvement over single-component models.

4. DISCUSSION

The preceding analysis shows that the most probable values for the thermal inertias of the bright and the dark areas of Mars are 0.004 and 0.006 cal cm^{-2} $sec^{-1/2}$ deg^{-1}, respectively. These values characterize the top 2 or 3 cm of the epilith. For particulate matter, the density is likely to be of order 2 g cm^{-3}, and the specific heat capacity, 0.15 cal g^{-1} deg^{-1}. The values of thermal conductivity corresponding to these two inertias are then 5×10^{-5} and 12×10^{-5} cal cm^{-1} sec^{-1} deg^{-1}.

Leovy (1966) has summarized a number of experimental determinations of thermal conductivity of mineral powders as a function of atmospheric pressure. At the Martian pressure of 10 mb, these conductivities depend strongly on particle size but not on composition. For the two values of the conductivity quoted above, the mean particle sizes are 20 to 40 μ and 100 to 150 μ for the bright and the dark areas, respectively. If, as suggested by Sagan and Pollack (1968), the dark areas are highlands with typical pressures of only 5 mb, then the derived particle sizes are increased to 200 to 300 μ. These sizes are considerably larger than those given by Leovy, since his value for the Martian thermal inertia was smaller than that found here. They are, however, in excellent agreement with the sizes of 25 μ and 80 to 400 μ obtained for the bright and the dark areas by Pollack and Sagan (1967) from an analysis of Martian photometry and polarimetry.

The equatorial minimum temperatures on Mars are probably between 175 and 185°K, somewhat lower than earlier estimates. At 180°K, the vapor pressure of water is 5×10^{-2} dyn cm^{-2}, or 5×10^{-6} of the 10-mb atmospheric pressure. The spectroscopic studies of Kaplan, Munch, and Spinrad (1964) and of Schorn, Spinrad, Moore, Smith, and Giver (1967) indicate that the water-vapor content of the Martian atmosphere is typically about 10^{-3} g cm^{-2}. Assuming that this water vapor is concentrated in the lower few kilometers of the troposphere, the water-vapor mixing ratio is of order 10^{-4} and the saturation vapor pressure is reached at a temperature of about 200°K. Thus, on the equator, frost can be expected to form after sunset and to persist until an hour or so after sunrise, where it may be identified with the dawn haze. De Vaucouleurs (1954) reports that the dawn haze sometimes persists until midmorning; whether such behavior will occur in the temperature regime discussed here depends on the quantity of frost deposited and on the evaporation rate, both of which are strongly dependent on the details of atmospheric turbulent diffusion near the surface. In view of the afternoon temperatures predicted in Figure 9, it seems unlikely that water vapor could condense to form the midafternoon clouds reported by many observers (see, e.g., de Vaucouleurs, 1954; Slipher, 1962).

The quantitative results presented here for Martian temperatures and thermal properties are ultimately based upon the accuracy of the absolute-temperature calibration for the center of the disk obtained by Sinton and Strong (1960a). As is shown in Figure 7, an error of a few degrees in the peak temperature will make a substantial difference in the deduced thermal inertia. It is encouraging, however, that the thermal inertia derived from Figure 7 for a peak temperature of 303°K also generates a theoretical curve that is in good agreement with the data over the entire observed range of solar hour angle without any *ad hoc* assumptions being necessary. While the results also depend strongly on the choice of bolometric albedos, the latter are now known with sufficient accuracy. The emissivities are less certain, but the results are affected little by the choice of alternative values.

Since more data have been utilized, the temperature results presented here are of higher accuracy than those given in previous studies. Through the use of currently accepted values for the albedo and emissivities of Mars and by carrying out theoretical computations for the exact latitude and heliocentric longitude of the planet at the time of the observations, I have obtained a satisfactory fit to these temperatures with a simple heat-conduction model. It thus seems unnecessary to use the more uncertain approach adopted by Leovy (1966), which depends on the application to Mars of a theory developed for the massive atmosphere of the earth. Also, the work of Gierasch and

Goody (1968) now strongly suggests that the atmosphere modifies only slightly the surface temperatures. Finally, I note that Gifford's temperatures (1956), based on the work of Lampland, are not compatible with the analysis presented here or with recent Mars temperatures derived by others.

In summary, the major conclusions from this analysis of Sinton and Strong's 1954 infrared scans of Mars are that

A. The observed Martian temperatures can be reproduced by a theoretical heat-conduction model employing a single, homogeneous surface layer.

B. For the bright areas, both the center-of-disk temperature given by Sinton and Strong and the variation of temperature with solar hour angle found here lead to a thermal inertia of 0.004 to 0.005 cal cm^{-2} $sec^{-1/2}$ deg^{-1}. The disk brightness temperature at radio wavelengths found by use of these inertias also agrees with the observations.

C. The darkest areas on the planet have noon temperatures 4° to 6° higher than the surrounding bright areas, indicative of a thermal inertia 0.001 to 0.002 larger than that of the bright areas.

D. The latitudinal temperature gradient is steeper in the Southern than in the Northern Hemisphere, consistent with the presence of a south polar cap of solid carbon dioxide.

E. The thermal inertias of bright and dark areas lead to estimates of mean particle sizes of 20 to 40 μ and 100 to 300 μ, respectively.

F. At the minimum equatorial temperatures of about 180°K, a major fraction of the atmospheric water vapor should condense each night.

5. ACKNOWLEDGMENTS

I wish to express my gratitude to Carl Sagan and James B. Pollack for suggesting this project and for offering constant advice and encouragement. I also thank Frank D. Drake, Peter Gierasch, Jeffrey L. Linsky, Nancy D. Morrison, and Richard Munro for many useful discussions, and I thank William Sinton for critically reading the manuscript.

REFERENCES

DENT, W. A., KLEIN, M. J. and ALLER, H. D.

1965. Measurements of Mars at λ 3.75 cm from February to June, 1965. Astrophys. Journ., vol. 142, pp. 1685-1688.

GIERASCH, P. and GOODY, R.

1968. A study of the thermal and dynamical structure of the Martian lower atmosphere. Planet. Space Sci., vol. 16, pp. 615-646.

GIFFORD, F. Jr.

1956. The surface-temperature climate of Mars. Astrophys. Journ., vol. 123, pp. 154-161.

GOLDSTEIN, R. M.

1965. Mars: radar observation. Science, vol. 150, pp. 1715-1717.

HOVIS, W. A. Jr. and CALLAHAN, W. R.

1966. Infrared reflectance spectra of igneous rocks, tuffs, and red sandstones from 0.5 to 22 μ. Journ. Opt. Soc. Amer., vol. 56, p. 639.

JAEGER, J. C.

1953. Surface temperature of the moon. Austral. Journ. Phys., vol. 6, p. 10.

JOHNSON, D. L.

1968. Lunar soil: Should this term be used? Science, vol. 160, p. 1258.

KAPLAN, L. D., MÜNCH, G. and SPINRAD, H.

1964. An analysis of the spectrum of Mars. Astrophys. Journ., vol. 139, pp. 1-15.

LEIGHTON, R. B. and MURRAY, B. C.

1966. Behavior of carbon dioxide and other volatiles on Mars. Science, vol. 153, pp. 136-144.

LEOVY, C.

1966. Note on thermal properties of Mars. Icarus, vol. 5, pp. 1-6.

LINSKY, J. L.

1966. Models of the lunar surface including temperature-dependent thermal properties. Icarus, vol. 5, pp. 606-634.

LOWELL, P.

1906. Mars and Its Canals. Macmillan, London, 393 pp.

McCORD, T. B.

1968. Differential colorimetry of Mars. Paper presented at AAS meeting, April 1968, Charlottesville, Va.

MORRISON, D. and SAGAN, C.

1967. The microwave phase effect of Mercury. Astrophys. Journ., vol. 150, pp. 1105-1110.

POLLACK, J. B. and SAGAN, C.

1967. An analysis of Martian photometry and polarimetry. Smithsonian Astrophys. Obs. Spec. Rep. No. 258, 96 pp.

REA, D. G., HETHERINGTON, H. and MIFFLIN, R.

1964. The analysis of radar echoes from the moon. Journ. Geophys. Res., vol. 69, pp. 5217-5223.

SAGAN, C. and POLLACK, J. B.

1968. Elevation differences on Mars. Journ. Geophys. Res., vol. 73, pp. 1373-1388.

SCHORN, R. A., SPINRAD, H., MOORE, R. C., SMITH, H. J. and GIVER, L. P.

1967. High-dispersion spectroscopic observations of Mars. II. The water-vapor variations. Astrophys. Journ., vol. 147, pp. 743-752.

SINTON, W.

1962. Temperatures on the lunar surface. <u>In</u> Physics and Astronomy of the Moon, edited by Z. Kopal, Academic Press, New York, pp. 407-428.

SINTON, W. M. and STRONG, J.

1960a. Radiometric observations of Mars. Astrophys. Journ., vol. 131, pp. 459-469.

1960b. Radiometric observations of Venus. Astrophys. Journ., vol. 131, pp. 470-490.

SINTON, W. M. and STRONG, J.
1960c. Observations of the infrared emission of planets and determination of their temperatures. Office of Naval Research Contract Report Nonr 248(01).

SLIPHER, E. C.
1962. The Photographic Story of Mars, edited by J. S. Hall. Sky Publ. Corp., Cambridge, Mass., and Northland Press, Flagstaff, Ariz., 168 pp.

DE VAUCOULEURS, G. P.
1954. Physics of the Planet Mars. Faber and Faber, Ltd., London, 365 pp.
1964. Geometric and photometric parameters of the terrestrial planets. Icarus, vol. 3, p. 187.

WALKER, R.
1966. Infrared photometry of stars and planets. Ph. D. thesis, Harvard University, Cambridge, Mass., 190 pp.

WALLACE, A. R.
1907. Is Mars Habitable? Macmillan, London, 110 pp.

WESSELINK, A. J.
1948. Heat conductivity and the nature of the lunar surface material. Bull. Astron. Inst. Neth., vol. 10, p. 351.

APPENDIX A

TRANSFORMATION TO AREOGRAPHIC COORDINATES

We wish to make a transformation from Cartesian coordinates (x, y) centered on a planetary disk of unit radius to the spherical coordinate system of the planet itself. Let us consider the planetary disk as it appears in an astronomical telescope, with celestial south at the top in the positive y direction, and east to the right in the positive x direction.

The first transformation is a rotation in the plane of the sky to coordinate axes aligned not with the celestial cardinal points but with the projection onto the celestial sphere of the planetary axis of rotation. The angle of rotation is the position angle (PA) of the planetary axis as given in the American Ephemeris, defined as "the angle which the meridian from the central point of the disk to the north pole of rotation forms with the declination circle through the central point, measured eastward from the north point of the disk." The new coordinates (x', y') are given by

$$x' = x \cos(PA) - y \sin(PA)$$

$$y' = y \cos(PA) + x \sin(PA) \quad .$$

The next step is to rotate about the x' axis so as to bring the projected rotation axis (y') into coincidence with the true axis (Y). Retaining Cartesian coordinates, we define

$$z'^2 \equiv 1 - x'^2 - y'^2 \quad .$$

The angle of rotation is given in the Ephemeris as D_e, the "planetocentric declination of the Earth." The transformation equations are

$$X = x'$$

$$Y = y' \cos(D_e) - z' \sin(D_e)$$

$$Z = z' \cos(D_e) + y' \sin(D_e) \quad .$$

If we identify the positive Y axis with the south pole, the transformation to spherical coordinates is

$$\phi = -\sin^{-1}(Y)$$

$$\theta = \tan^{-1}\left(\frac{X}{Z}\right) \quad ,$$

where ϕ is the latitude and $\theta = 0$ on the central meridian. To determine the longitude λ of a point, we must use the Ephemeris value for the longitude of the central meridian of the time of observation.

Other parameters of interest for each point on the planet are the solar hour angle (LHA), the elevation angle of the sun (α_s), and the elevation angle of the earth (α_e). These are given by

$$LHA = -(\theta + i)$$

$$\alpha_s = \sin^{-1}[\sin(\phi)\sin(D_s) + \cos(\phi)\cos(D_s)\cos(LHA)]$$

$$\alpha_e = \sin^{-1}(z) \quad ,$$

where the phase angle i and the planetocentric declination of the sun D_s are both listed in the Ephemeris.

APPENDIX B

DATA LISTING

Listed in this appendix are the reduced temperature data obtained from the analog records given by Sinton and Strong (1960c). Two of the 33 scans given there have not been included: scan 4 on July 20, because of inconsistent indications of position on the disk, and scan 6 on July 21, because it only grazed the limb of the planet and could not be normalized.

For each scan, the following information is given: The first column, D, is the deflection of the radiometer on an arbitrary scale. The brightness temperature, TEMP, in K° is that described in the text. The columns X and Y are the Cartesian coordinates of the point; the disk was taken to have a radius of 100 and to have the planetary south direction toward positive Y. The areographic coordinates of the point are labeled LAT and LONG, and LHA is the solar hour angle. The final column gives the nature of the area under observation: off the planet (SKY), bright area or mixed area (LGHT), Meridiani Sinus (MERI), Margaritifer Sinus (MARG), Syrtis Major (S. M.), or the suspected yellow cloud on July 20 (CLD). The times, central meridians, and zenith distances for each scan were given by Sinton and Strong (1960c).

MARS DATA, JULY 20, SCAN 1

D	TEMP	X	Y	LAT	LONG	LHA	AREA
3	201	-106	-20				SKY
8	235	-98	-18				SKY
18	270	-90	-16	11	296	48	LGHT
24	286	-82	-16	11	305	39	LGHT
27	293	-75	-14	11	312	31	LGHT
28	296	-65	-14	11	320	24	LGHT
29	298	-57	-12	10	326	18	LGHT
29	298	-49	-10	9	332	11	LGHT
30	300	-41	-10	10	337	7	LGHT
28	296	-31	-8	9	343	1	LGHT
27	293	-24	-8	9	348	-4	LGHT
26	291	-16	-6	8	353	-9	LGHT
26	291	-8	-6	8	357	-14	LGHT
24	286	0	-4	7	2	-18	LGHT
21	279	10	-2	5	7	-23	LGHT
18	270	18	0	4	11	-28	LGHT
17	267	25	0	4	17	-33	LGHT
14	258	33	2	3	21	-38	MARG
12	251	43	4	2	27	-43	MARG
8	235	51	4	1	32	-48	LGHT
8	235	59	6	0	38	-54	LGHT
5	220	67	6	-0	44	-60	LGHT
4	212	76	8	-2	52	-68	LGHT
3	201	84	8	-2	59	-75	LGHT
1	174	92	10	-4	71	-87	LGHT

MARS DATA, JULY 20, SCAN 2

D	TEMP	X	Y	LAT	LONG	LHA	AREA
2	202	-78	-63				SKY
4	226	-71	-63	41	296	50	CLD
12	271	-63	-61	40	309	37	CLD
13	275	-55	-61	40	318	28	LGHT
14	279	-47	-59	39	327	20	LGHT
13	275	-39	-59	40	333	13	LGHT
15	283	-31	-59	40	340	6	LGHT
16	287	-24	-57	39	347	-0	LGHT
15	283	-16	-57	39	353	-6	LGHT
15	283	-8	-55	38	358	-12	LGHT
13	275	0	-55	38	4	-18	LGHT
10	262	8	-55	38	10	-24	LGHT
8	251	16	-53	36	15	-29	LGHT
7	246	24	-53	36	21	-35	LGHT
5	233	31	-51	35	27	-40	LGHT
4	226	39	-51	34	33	-46	LGHT
3	217	47	-49	33	38	-52	LGHT
2	202	55	-49	33	45	-59	LGHT
1	182	63	-47	31	51	-65	LGHT
0	0	71	-47	31	59	-73	LGHT
0	0	78	-45	29	68	-81	LGHT

MARS DATA, JULY 20, SCAN 3

D	TEMP	X	Y	LAT	LONG	LHA	AREA
2	187	-96	31				SKY
16	260	-88	31	-17	299	49	LGHT
18	266	-80	31	-16	309	39	LGHT
28	291	-71	31	-15	319	29	LGHT
32	299	-63	31	-15	326	23	LGHT
31	297	-53	33	-16	333	15	LGHT
31	297	-45	33	-16	338	10	LGHT
32	299	-35	33	-15	345	4	LGHT
31	297	-27	33	-15	350	-1	LGHT
31	297	-18	33	-15	356	-7	LGHT
29	293	-10	33	-15	0	-12	LGHT
26	286	-2	33	-15	5	-17	LGHT
25	284	6	33	-15	10	-21	LGHT
22	277	16	33	-15	15	-27	LGHT
21	274	27	33	-15	23	-34	MARG
18	266	35	35	-17	28	-40	LGHT
15	257	45	35	-17	34	-46	LGHT
11	244	53	35	-17	40	-52	LGHT
9	236	63	35	-17	47	-59	LGHT
6	223	71	35	-18	54	-66	LGHT
4	208	80	35	-18	64	-76	LGHT
3	199	88	35	-19	75	-87	LGHT
1	173	96	35				SKY

MARS DATA, JULY 20, SCAN 5

D	TEMP	X	Y	LAT	LONG	LHA	AREA
3	195	-106	8				SKY
6	219	-96	8	-3	296	56	LGHT
20	265	-88	8	-2	308	44	LGHT
26	279	-78	8	-2	318	34	LGHT
32	291	-71	8	-1	325	27	LGHT
34	295	-61	10	-2	332	20	LGHT
37	300	-53	10	-2	338	14	LGHT
37	300	-43	10	-2	344	8	LGHT
36	298	-33	10	-2	350	2	LGHT
35	296	-25	10	-1	355	-3	LGHT
34	295	-18	12	-3	360	-8	MERI
32	291	-8	12	-2	5	-13	LGHT
29	285	2	12	-2	11	-19	LGHT
26	279	10	12	-2	15	-24	LGHT
23	272	18	12	-3	20	-28	MARG
21	267	27	14	-4	26	-34	MARG
18	260	37	14	-4	32	-40	LGHT
14	248	45	14	-4	37	-45	LGHT
12	242	55	14	-4	43	-51	LGHT
9	232	63	14	-5	49	-57	LGHT
5	212	73	14	-5	57	-65	LGHT
3	195	80	16	-7	64	-72	LGHT
2	184	90	16	-7	75	-83	LGHT

MARS DATA, JULY 20, SCAN 6

D	TEMP	X	Y	LAT	LONG	LHA	AREA
3	195	94	-35				SKY
2	184	-94	-31	19	288	66	CLD
12	242	-86	-31	20	305	49	CLD
21	267	-76	-31	21	317	37	CLD
25	276	-69	-31	21	325	30	CLD
29	285	-59	-33	23	332	22	LGHT
29	285	-49	-33	23	340	14	LGHT
32	291	-39	-33	23	347	7	LGHT
32	291	-29	-33	24	353	1	LGHT
31	289	-20	-33	24	360	-6	LGHT
30	287	-10	-33	24	6	-12	LGHT
29	285	0	-33	24	12	-18	LGHT
25	276	10	-33	24	18	-24	LGHT
23	272	20	-33	24	24	-30	LGHT
20	265	29	-33	24	31	-37	LGHT
17	257	39	-33	23	37	-43	LGHT
13	245	49	-33	23	44	-50	LGHT
11	239	59	-35	24	52	-58	LGHT
10	235	69	-35	24	60	-66	LGHT
8	228	76	-35	23	68	-74	LGHT
5	212	86	-35	22	81	-87	LGHT

MARS DATA, JULY 20, SCAN 7

D	TEMP	X	Y	LAT	LONG	LHA	AREA
1	175	-73	-73				SKY
3	203	-65	-73	48	299	57	CLD
5	221	-53	-73	49	320	36	LGHT
6	227	-43	-73	50	332	24	LGHT
7	232	-33	-75	52	341	15	LGHT
6	227	-24	-75	52	351	5	LGHT
8	236	-16	-75	52	359	-3	LGHT
8	236	-8	-75	52	6	-11	LGHT
6	227	0	-75	52	14	-18	LGHT
5	221	8	-75	52	21	-25	LGHT
3	203	16	-75	52	29	-33	LGHT
4	213	24	-76	54	37	-41	LGHT
3	203	31	-76	54	46	-50	LGHT
3	203	39	-76	53	55	-59	LGHT
3	203	49	-76	53	67	-72	LGHT

MARS DATA, JULY 20, SCAN 8

D	TEMP	X	Y	LAT	LONG	LHA	AREA
1	172	-103	-16				SKY
11	241	-93	-16	11	304	53	LGHT
23	275	-85	-14	10	316	42	LGHT
30	291	-75	-14	11	326	32	LGHT
31	293	-65	-14	11	334	24	LGHT
34	298	-57	-12	10	340	18	LGHT
35	300	-50	-12	11	345	12	LGHT
34	298	-40	-12	11	352	6	LGHT
35	300	-30	-10	10	358	-0	LGHT
33	297	-20	-10	10	4	-6	LGHT
30	291	-10	-10	10	10	-12	LGHT
29	289	0	-8	9	16	-18	LGHT
26	282	10	-8	9	21	-24	LGHT
22	273	20	-6	8	27	-29	LGHT
17	260	30	-6	8	33	-35	LGHT
16	257	40	-4	6	39	-41	LGHT
14	251	51	-4	6	47	-49	LGHT
12	245	61	-2	5	54	-56	LGHT
9	234	71	-2	4	61	-64	LGHT
3	197	81	0	3	70	-72	LGHT
1	172	91	0	2	81	-84	LGHT
0	0	101	0				SKY

MARS DATA, JULY 20, SCAN 9

D	TEMP	X	Y	LAT	LONG	LHA	AREA
0	0	-25	100				SKY
0	0	-25	92	-64	344	17	LGHT
1	172	-27	84	-54	351	10	LGHT
10	238	-27	75	-44	356	5	LGHT
22	273	-29	67	-38	357	4	LGHT
26	283	-29	57	-31	359	2	LGHT
31	293	-31	49	-25	358	2	LGHT
30	291	-31	41	-20	359	2	LGHT
32	295	-33	31	-14	359	2	LGHT
35	301	-33	24	-10	359	2	MERI
38	306	-35	16	-5	358	3	MERI
35	301	-35	6	1	358	3	MERI
32	295	-37	-2	5	357	4	LGHT
32	295	-37	-12	11	357	4	LGHT
33	297	-39	-20	15	355	6	LGHT
31	293	-39	-29	21	354	7	LGHT
27	285	-41	-37	26	352	9	LGHT
27	285	-41	-45	31	350	11	LGHT
22	273	-43	-53	36	347	14	LGHT
18	263	-43	-61	41	344	17	LGHT
12	245	-45	-71	48	336	25	LGHT
5	215	-45	-78	54	328	33	LGHT

MARS DATA, JULY 20, SCAN 10

D	TEMP	X	Y	LAT	LONG	LHA	AREA
4	205	-20	84	-53	2	1	LGHT
20	266	-24	76	-46	1	2	LGHT
24	276	-25	69	-39	2	1	LGHT
28	284	-25	61	-33	3	-0	LGHT
31	290	-27	53	-28	3	0	LGHT
33	294	-29	45	-23	2	1	LGHT
35	298	-31	35	-17	2	1	LGHT
37	301	-33	25	-11	1	2	LGHT
40	306	-35	18	-6	360	3	MERI
40	306	-37	8	-1	359	4	MERI
36	300	-39	0	4	358	5	LGHT
35	298	-41	-8	8	356	7	LGHT
36	300	-43	-18	14	354	8	LGHT
33	294	-45	-25	19	352	11	LGHT
32	292	-47	-33	23	350	13	LGHT
26	280	-47	-43	29	348	15	LGHT
23	273	-49	-51	34	344	18	LGHT
17	258	-51	-59	39	340	23	LGHT
12	243	-51	-69	46	333	30	LGHT
10	236	-53	-76	52	321	42	LGHT
3	195	-55	-84				SKY

MARS DATA, JULY 20, SCAN 11

D	TEMP	X	Y	LAT	LONG	LHA	AREA
3	184	-78	71				SKY
3	184	-78	61	-37	305	60	LGHT
9	220	-80	53	-31	314	51	LGHT
15	236	-80	43	-24	321	43	LGHT
21	249	-82	35	-19	322	42	LGHT
30	265	-82	25	-12	325	40	LGHT
35	273	-84	18	-8	324	40	LGHT
34	272	-86	8	-2	323	42	LGHT
28	262	-88	0	2	320	44	LGHT
22	251	-88	-8	6	320	45	LGHT
13	231	-90	-18	12	315	49	LGHT
14	233	-90	-25	16	312	52	CLD
14	233	-92	-35	21	301	64	CLD
10	223	-94	-43				SKY
3	184	-94	-53				SKY

MARS DATA, JULY 20, SCAN 12

D	TEMP	X	Y	LAT	LONG	LHA	AREA
4	205	-49	82	-53	329	37	LGHT
8	229	-49	73	-43	341	25	LGHT
19	265	-49	63	-35	347	19	LGHT
22	272	-51	55	-30	348	18	LGHT
22	272	-51	47	-25	350	16	LGHT
27	284	-53	37	-18	350	16	LGHT
33	296	-53	27	-12	351	15	LGHT
35	299	-53	20	-8	351	14	LGHT
37	303	-55	12	-3	350	15	LGHT
35	299	-55	2	2	350	15	LGHT
33	296	-55	-6	7	350	16	LGHT
26	281	-57	-24	17	347	19	LGHT
24	277	-57	-31	22	346	20	LGHT
18	262	-57	-41	28	344	22	LGHT
16	256	-59	-49	32	339	26	LGHT
7	225	-59	-59	39	335	31	LGHT
1	172	-59	-69	46	326	40	LGHT

MARS DATA, JULY 20, SCAN 13

D	TEMP	X	Y	LAT	LONG	LHA	AREA
0	0	10	94	-66	40	-32	LGHT
0	0	8	86	-55	34	-26	LGHT
3	197	6	78	-47	31	-23	LGHT
14	252	4	69	-39	29	-21	LGHT
20	269	2	61	-33	27	-19	LGHT
23	277	0	53	-28	26	-18	LGHT
27	286	0	43	-21	26	-18	LGHT
30	292	-2	35	-16	25	-17	LGHT
33	298	-4	25	-10	24	-16	MARG
33	298	-6	18	-6	22	-15	MARG
31	294	-8	8	-0	21	-13	MARG
30	292	-10	0	4	20	-12	MARG
30	292	-12	-8	9	19	-11	LGHT
28	288	-14	-18	14	18	-10	LGHT
28	288	-16	-25	19	16	-8	LGHT
28	288	-16	-35	25	16	-8	LGHT
27	286	-18	-43	30	14	-6	LGHT
23	277	-20	-53	36	12	-4	LGHT
19	267	-22	-61	42	9	-1	LGHT
15	255	-24	-69	47	6	2	LGHT
11	242	-25	-78	56	359	9	LGHT
5	215	-27	-86	63	348	20	LGHT
3	197	-29	-94	72	314	54	LGHT

MARS DATA, JULY 20, SCAN 14

D	TEMP	X	Y	LAT	LONG	LHA	AREA
2	183	49	100				SKY
2	183	47	92				SKY
3	193	45	84	-55	79	-70	LGHT
6	218	43	76	-47	66	-57	LGHT
11	237	41	67	-38	59	-49	LGHT
14	247	39	57	-31	55	-45	LGHT
15	250	37	49	-25	52	-42	LGHT
19	261	35	41	-20	50	-40	LGHT
22	268	33	31	-14	48	-38	LGHT
23	270	31	22	-8	46	-36	LGHT
22	268	29	14	-4	45	-35	LGHT
22	268	29	4	2	45	-35	LGHT
23	270	27	-4	6	44	-34	LGHT
22	268	25	-14	12	43	-33	LGHT
20	263	24	-22	17	42	-32	LGHT
19	261	22	-31	22	41	-31	LGHT
18	258	20	-41	29	40	-31	LGHT
14	247	18	-47	32	40	-30	LGHT
12	241	16	-55	38	39	-29	LGHT
8	227	14	-65	45	39	-29	LGHT
6	218	12	-75	52	39	-29	LGHT
3	193	10	-82	60	39	-29	LGHT

MARS DATA, JULY 21, SCAN 1

D	TEMP	X	Y	LAT	LONG	LHA	AREA
2	179	-37	102				SKY
10	229	-41	92				SKY
18	251	-43	82	-53	304	27	LGHT
25	266	-47	75	-45	307	24	LGHT
30	276	-49	65	-37	311	20	LGHT
33	281	-53	55	-30	311	20	LGHT
36	286	-57	45	-23	311	20	LGHT
39	291	-61	35	-17	309	22	LGHT
40	292	-65	25	-12	307	23	LGHT
40	292	-67	16	-6	307	24	LGHT
39	291	-71	6	-0	304	27	LGHT
38	289	-73	-4	5	302	29	LGHT
36	286	-76	-14	11	298	33	LGHT
32	279	-80	-24	16	292	39	LGHT
27	270	-82	-33	22	287	44	LGHT
20	255	-86	-43	27	274	57	LGHT
14	240	-90	-53				SKY
6	211	-94	-63				SKY
1	168	-96	-73				SKY

MARS DATA, JULY 21, SCAN 2

D	TEMP	X	Y	LAT	LONG	LHA	AREA
2	181	-37	84	-54	311	22	LGHT
15	246	-39	76	-46	316	17	LGHT
29	278	-39	67	-38	321	12	LGHT
32	283	-41	57	-31	322	11	LGHT
34	287	-43	51	-27	322	11	LGHT
38	293	-45	37	-18	322	10	LGHT
41	298	-47	27	-12	322	11	LGHT
43	301	-49	18	-6	321	12	LGHT
42	300	-49	8	-1	321	11	LGHT
40	297	-51	0	4	320	13	LGHT
39	295	-53	-8	8	318	14	LGHT
37	292	-55	-18	14	316	17	LGHT
34	287	-57	-27	19	314	19	LGHT
30	279	-59	-37	25	310	23	LGHT
25	270	-59	-51	34	306	27	LGHT
20	259	-61	-57	37	301	32	LGHT
16	249	-63	-67	44	290	43	LGHT
7	220	-65	-76				SKY
3	191	-67	-84				SKY

MARS DATA, JULY 21, SCAN 3

D	TEMP	X	Y	LAT	LONG	LHA	AREA
1	173	45	82	-53	41	-66	LGHT
5	217	45	73	-43	31	-56	LGHT
8	232	43	65	-37	26	-50	LGHT
12	247	43	55	-30	23	-48	LGHT
13	251	41	45	-23	20	-44	LGHT
17	263	39	37	-18	18	-42	LGHT
18	266	39	27	-12	17	-42	LGHT
19	269	37	18	-6	15	-40	LGHT
18	266	35	8	-0	14	-39	LGHT
18	266	35	-2	5	14	-39	LGHT
19	269	33	-12	11	13	-38	LGHT
19	269	31	-22	17	12	-37	LGHT
17	263	29	-27	20	11	-36	LGHT
17	263	29	-37	26	12	-37	LGHT
14	254	27	-47	32	12	-37	LGHT
11	244	27	-57	39	14	-38	LGHT
7	228	25	-63	43	14	-38	LGHT
3	198	25	-75	52	18	-42	LGHT
1	173	24	-84	61	23	-47	LGHT
0	0	24	-94	73	47	-72	LGHT

MARS DATA, JULY 21, SCAN 4

D	TEMP	X	Y	LAT	LONG	LHA	AREA
1	169	4	98	-74	3	-26	LGHT
7	219	2	88	-58	357	-20	LGHT
17	250	0	78	-47	355	-18	LGHT
27	272	-2	69	-39	353	-16	LGHT
29	276	-4	59	-32	352	-15	LGHT
32	281	-4	49	-25	352	-15	LGHT
35	287	-6	39	-19	351	-14	LGHT
38	291	-8	29	-13	350	-13	LGHT
40	295	-10	20	-7	349	-12	LGHT
41	296	-12	10	-1	348	-11	LGHT
41	296	-14	0	4	347	-10	LGHT
40	295	-16	-10	10	346	-9	LGHT
39	293	-18	-20	16	344	-7	LGHT
35	287	-20	-29	21	343	-6	LGHT
31	280	-22	-39	27	341	-4	LGHT
26	270	-24	-49	33	339	-2	LGHT
19	255	-25	-59	40	335	2	LGHT
13	239	-27	-69	47	331	6	LGHT
6	213	-29	-78	55	324	13	LGHT
4	199	-31	-88	65	307	30	LGHT
2	180	-33	-98				SKY

MARS DATA, JULY 21, SCAN 5

D	TEMP	X	Y	LAT	LONG	LHA	AREA
1	169	-45	88	-60	291	48	LGHT
3	190	-47	78	-49	311	28	LGHT
12	236	-47	69	-40	319	20	LGHT
22	261	-49	59	-33	321	18	LGHT
31	279	-49	49	-26	324	15	LGHT
35	286	-53	39	-20	322	16	LGHT
37	289	-53	29	-14	324	15	LGHT
40	294	-55	20	-8	323	16	LGHT
42	297	-57	10	-2	322	17	LGHT
41	296	-59	0	3	321	18	LGHT
40	294	-59	-10	9	320	19	LGHT
39	293	-61	-20	15	318	21	LGHT
36	288	-61	-29	20	316	23	LGHT
31	279	-63	-39	26	312	26	LGHT
27	272	-63	-49	32	309	30	LGHT
21	259	-65	-59	39	301	38	LGHT
14	242	-67	-69	45	286	52	LGHT
8	223	-69	-78				SKY
3	190	-69	-88				SKY

MARS DATA, JULY 21, SCAN 7

D	TEMP	X	Y	LAT	LONG	LHA	AREA
1	168	-62	74	-46	297	45	LGHT
4	197	-64	66	-39	305	37	LGHT
12	235	-66	60	-34	307	35	LGHT
24	264	-68	54	-30	309	34	LGHT
34	282	-70	48	-26	309	33	LGHT
36	286	-72	42	-22	309	33	LGHT
36	286	-74	36	-18	309	33	LGHT
37	287	-74	30	-15	311	32	LGHT
37	287	-76	22	-10	310	33	LGHT
37	287	-78	16	-7	309	34	LGHT
34	282	-80	10	-3	307	35	LGHT
32	279	-82	4	0	305	37	LGHT
28	272	-84	-4	5	303	40	LGHT
23	262	-86	-10	8	300	42	LGHT
18	250	-88	-16	11	297	46	LGHT
16	245	-90	-22	14	292	50	LGHT
3	189	-72	-30	20	310	32	LGHT
1	168	-94	-36				SKY

MARS DATA, JULY 21, SCAN 8

D	TEMP	X	Y	LAT	LONG	LHA	AREA
1	171	32	90	-61	43	-59	LGHT
2	183	32	82	-51	33	-49	LGHT
9	231	32	72	-42	28	-43	LGHT
12	242	32	62	-34	25	-41	LGHT
15	251	32	52	-27	23	-39	LGHT
19	262	32	42	-21	22	-38	LGHT
22	269	32	32	-15	21	-37	MARG
23	271	32	20	-7	21	-37	MARG
24	274	32	10	-2	21	-37	MARG
21	267	32	0	4	21	-37	MARG
21	267	32	-8	9	21	-37	LGHT
21	267	32	-18	14	21	-37	LGHT
20	264	32	-26	19	22	-38	LGHT
18	259	32	-36	25	23	-39	LGHT
14	248	32	-44	30	24	-40	LGHT
11	238	32	-54	37	25	-41	LGHT
8	227	32	-62	42	28	-44	LGHT
4	203	32	-72	50	32	-48	LGHT
3	194	32	-82	59	40	-56	LGHT
1	171	32	-90	67	57	-72	LGHT

MARS DATA, JULY 21, SCAN 9

D	TEMP	X	Y	LAT	LONG	LHA	AREA
7	219	-103	-2				SKY
22	262	-95	-2	2	292	54	LGHT
34	285	-85	-2	3	305	41	LGHT
39	293	-73	-2	4	317	29	LGHT
40	295	-63	-2	4	324	22	LGHT
41	296	-51	-4	6	333	13	LGHT
44	301	-44	-4	6	338	8	LGHT
43	299	-32	-4	6	345	1	LGHT
40	295	-22	-4	6	351	-5	LGHT
38	291	-12	-4	7	357	-11	LGHT
34	285	-2	-4	7	3	-17	LGHT
32	281	8	-4	7	9	-22	LGHT
28	274	18	-4	7	14	-28	LGHT
26	270	26	-4	6	19	-33	LGHT
24	266	38	-4	6	26	-40	LGHT
20	257	48	-6	7	33	-47	LGHT
18	252	57	-6	7	39	-53	LGHT
13	239	65	-6	7	45	-59	LGHT
11	233	75	-6	6	53	-67	LGHT
7	219	83	-6	6	61	-75	LGHT
5	206	93	-6	5	73	-87	LGHT
3	190	101	-6				SKY

MARS DATA, JULY 23, SCAN 1

D	TEMP	X	Y	LAT	LONG	LHA	AREA
2	193	-108	-18				SKY
4	217	-100	-18				SKY
10	249	-94	-18	12	259	52	LGHT
13	261	-86	-16	11	270	41	LGHT
17	275	-78	-16	12	278	33	S.M.
20	284	-70	-16	12	285	26	S.M.
23	292	-62	-16	13	291	20	S.M.
24	295	-54	-16	13	298	13	LGHT
25	297	-46	-14	12	303	8	LGHT
24	295	-36	-14	12	309	2	LGHT
25	297	-28	-14	12	314	-3	LGHT
25	297	-22	-14	12	319	-8	LGHT
26	300	-12	-14	13	324	-13	LGHT
24	295	-4	-12	11	329	-18	LGHT
22	289	6	-12	11	334	-23	LGHT
19	281	14	-12	11	340	-29	LGHT
16	271	22	-12	11	344	-34	LGHT
15	268	30	-10	10	349	-38	LGHT
12	257	38	-10	10	354	-43	LGHT
10	249	48	-10	10	360	-49	LGHT
9	245	56	-10	9	6	-55	LGHT
6	230	64	-10	9	12	-61	LGHT
5	224	74	-8	8	19	-68	LGHT
3	206	82	-8	7	26	-75	LGHT
3	206	90	-8	7	35	-84	LGHT
2	193	96	-8	6	47	-97	LGHT

MARS DATA, JULY 23, SCAN 2

D	TEMP	X	Y	LAT	LONG	LHA	AREA
7	230	-92	-20	13	262	51	LGHT
16	264	-84	-20	14	273	40	LGHT
21	279	-76	-20	14	282	31	S.M.
26	291	-68	-18	14	289	24	S.M.
27	293	-60	-18	14	295	18	LGHT
29	298	-52	-18	14	301	12	LGHT
28	296	-42	-18	14	308	6	LGHT
30	300	-34	-18	15	313	0	LGHT
30	300	-26	-18	15	318	-5	LGHT
28	296	-18	-18	15	323	-9	LGHT
28	296	-8	-18	15	328	-15	LGHT
27	293	0	-16	14	333	-20	LGHT
25	289	10	-16	14	339	-26	LGHT
23	284	20	-16	14	345	-32	LGHT
21	279	28	-16	14	350	-37	LGHT
18	270	36	-16	13	355	-42	LGHT
15	261	44	-16	13	0	-47	LGHT
12	251	54	-16	13	7	-54	LGHT
10	243	62	-16	13	13	-60	LGHT
6	226	70	-14	11	19	-66	LGHT
4	211	80	-14	11	28	-75	LGHT
3	201	88	-14	10	37	-84	LGHT
1	174	96	-14	9	50	-97	LGHT
0	0	104	-14				SKY

MARS DATA, JULY 23, SCAN 3

D	TEMP	X	Y	LAT	LONG	LHA	AREA
3	198	-98	20				SKY
15	257	-90	20	-10	270	46	LGHT
23	279	-80	20	-9	282	34	LGHT
30	294	-70	20	-8	291	25	LGHT
33	300	-62	20	-8	297	19	LGHT
31	296	-52	20	-8	304	11	LGHT
32	298	-42	22	-9	311	5	LGHT
32	298	-34	22	-8	316	-0	LGHT
33	300	-24	22	-8	322	-6	LGHT
33	300	-16	22	-8	327	-11	LGHT
31	296	-6	22	-8	332	-17	LGHT
30	294	4	22	-8	338	-23	LGHT
26	286	12	24	-9	343	-27	LGHT
24	281	22	24	-10	349	-33	LGHT
21	274	32	24	-10	355	-39	LGHT
20	271	40	24	-10	360	-44	MERI
17	263	50	24	-10	6	-51	LGHT
12	247	60	24	-10	13	-58	LGHT
10	240	68	26	-12	20	-64	MARG
7	227	78	26	-12	29	-73	LGHT
5	217	88	26	-13	41	-85	LGHT
3	198	96	26	-15	59	-103	LGHT

MARS DATA, JULY 23, SCAN 4

D	TEMP	X	Y	LAT	LONG	LHA	AREA
1	172	-104	24				SKY
6	221	-94	24	-13	263	54	LGHT
21	270	-86	24	-12	276	41	LGHT
26	282	-78	24	-11	285	32	LGHT
31	293	-68	24	-11	294	24	LGHT
34	298	-58	24	-10	301	16	LGHT
35	300	-48	24	-10	308	9	LGHT
34	298	-40	24	-10	313	4	LGHT
33	296	-30	24	-10	320	-2	LGHT
33	296	-22	22	-8	325	-7	LGHT
32	294	-14	22	-8	329	-12	LGHT
30	291	-4	22	-8	335	-18	LGHT
28	286	4	22	-8	340	-23	LGHT
27	284	14	22	-8	346	-28	LGHT
25	280	24	22	-8	351	-34	LGHT
21	270	32	22	-8	356	-39	MERI
20	268	42	22	-9	3	-45	MERI
17	260	50	20	-8	8	-50	LGHT
14	251	60	20	-8	15	-57	LGHT
10	237	68	20	-8	21	-64	MARG
6	221	78	20	-9	29	-72	LGHT
4	206	86	20	-9	38	-81	LGHT
3	196	94	20	-10	50	-93	LGHT

MARS DATA, JULY 23, SCAN 5

D	TEMP	X	Y	LAT	LONG	LHA	AREA
0	0	-74	62	-37	272	47	LGHT
7	228	-64	60	-34	289	30	LGHT
15	257	-56	60	-34	297	22	LGHT
20	272	-48	58	-32	305	14	LGHT
22	277	-38	58	-31	313	6	LGHT
22	277	-30	56	-30	319	0	LGHT
27	289	-20	56	-30	326	-7	LGHT
30	295	-12	54	-28	332	-12	LGHT
18	266	-2	54	-28	338	-19	LGHT
26	286	6	52	-27	343	-24	LGHT
26	286	16	52	-27	350	-31	LGHT
25	284	24	50	-26	355	-36	LGHT
23	279	34	50	-26	2	-42	LGHT
19	269	42	50	-26	7	-48	LGHT
16	260	52	48	-25	14	-55	LGHT
15	257	60	48	-25	21	-62	LGHT
11	244	70	46	-25	30	-71	LGHT
9	236	78	46	-25	39	-80	LGHT
4	209	88	44	-25	56	-97	LGHT
3	199	96	44				SKY
1	173	104	42				SKY

MARS DATA, JULY 23, SCAN 7

D	TEMP	X	Y	LAT	LONG	LHA	AREA
1	175	-90	52				SKY
6	227	-80	52	-30	275	47	LGHT
15	263	-70	52	-29	290	33	LGHT
22	284	-60	52	-28	300	23	LGHT
23	286	-50	52	-28	308	14	LGHT
25	291	-40	52	-27	316	7	LGHT
25	291	-30	52	-27	323	-1	LGHT
25	291	-20	52	-27	330	-7	LGHT
24	289	-10	54	-28	336	-14	LGHT
21	281	0	54	-28	342	-20	LGHT
20	278	10	54	-28	349	-27	LGHT
17	270	20	54	-28	356	-33	LGHT
13	257	30	54	-28	2	-40	LGHT
11	249	40	54	-29	10	-47	LGHT
10	245	50	54	-29	17	-55	LGHT
6	227	60	54	-29	26	-64	LGHT
2	190	70	54	-30	37	-74	LGHT
2	190	80	54	-31	52	-89	LGHT
0	0	90	54				SKY

MARS DATA, JULY 28, SCAN 1

D	TEMP	X	Y	LAT	LONG	LHA	AREA
1	175	-16	90	-60	277	-4	LGHT
8	237	-20	80	-49	278	-5	LGHT
13	257	-24	68	-39	277	-5	LGHT
16	268	-26	58	-31	278	-5	LGHT
21	282	-30	46	-23	276	-4	LGHT
25	293	-34	34	-16	275	-2	LGHT
26	295	-38	22	-9	273	-0	LGHT
28	300	-42	10	-2	270	2	LGHT
27	297	-46	0	4	268	4	LGHT
26	295	-50	-10	10	265	7	LGHT
23	288	-54	-20	15	261	11	LGHT
22	285	-58	-30	21	257	15	LGHT
21	282	-60	-40	27	253	19	LGHT
19	277	-64	-50	33	246	27	LGHT
15	264	-70	-60	39	231	41	LGHT
8	237	-72	-70				SKY
5	222	-76	-80				SKY
1	175	-78	-90				SKY

MARS DATA, JULY 28, SCAN 2

D	TEMP	X	Y	LAT	LONG	LHA	AREA
0	0	-30	98				SKY
3	204	-30	86	-56	264	9	LGHT
15	265	-32	78	-47	268	5	LGHT
17	271	-32	68	-39	272	1	LGHT
19	277	-34	58	-31	273	0	LGHT
21	283	-34	50	-26	274	-1	LGHT
25	293	-36	40	-19	274	-1	LGHT
26	295	-36	30	-13	275	-1	LGHT
27	298	-38	20	-7	274	-0	LGHT
28	300	-38	12	-3	274	-1	LGHT
27	298	-40	2	3	273	1	LGHT
24	291	-40	-8	9	273	1	LGHT
24	291	-42	-18	14	271	3	LGHT
22	285	-42	-26	19	270	3	LGHT
20	280	-44	-36	25	267	6	LGHT
20	280	-44	-46	31	265	8	LGHT
18	274	-46	-56	38	261	13	LGHT
16	268	-46	-64	43	257	16	LGHT
14	261	-48	-74	51	247	26	LGHT
10	246	-48	-84	59	228	46	LGHT
6	228	-46	-94				SKY
3	204	-50	-102				SKY
1	175	-52	-112				SKY

MARS DATA, JULY 28, SCAN 4

D	TEMP	X	Y	LAT	LONG	LHA	AREA
0	0	12	98	-75	326	-50	LGHT
3	202	12	90	-60	313	-37	LGHT
8	235	12	82	-51	310	-34	LGHT
9	240	12	76	-45	309	-33	LGHT
11	248	10	68	-38	307	-30	LGHT
13	255	10	60	-32	306	-30	LGHT
15	262	10	52	-27	306	-29	LGHT
16	265	10	46	-23	306	-29	LGHT
17	268	10	38	-18	305	-29	LGHT
19	274	10	30	-13	305	-29	LGHT
20	277	10	22	-8	305	-29	LGHT
21	279	10	14	-4	305	-29	LGHT
22	282	10	8	-0	305	-29	LGHT
21	279	10	2	3	305	-29	LGHT
22	282	10	-6	8	305	-29	LGHT
23	285	8	-12	11	304	-28	LGHT
21	279	8	-20	16	304	-28	LGHT
22	282	8	-28	21	304	-28	LGHT
21	279	8	-36	26	304	-28	LGHT
18	271	8	-44	31	305	-28	LGHT
16	265	8	-50	34	305	-29	LGHT
13	255	8	-58	40	305	-29	LGHT
11	248	8	-66	46	306	-30	LGHT
9	240	8	-72	51	307	-30	LGHT
6	226	8	-80	58	308	-32	LGHT
2	189	6	-88	66	308	-32	LGHT
1	174	6	-96	78	316	-40	LGHT
0	0	6	-102				SKY

MARS DATA, JULY 28, SCAN 5

D	TEMP	X	Y	LAT	LONG	LHA	AREA
2	186	-54	90				SKY
4	208	-54	84	-56	223	55	LGHT
8	231	-54	78	-49	246	32	LGHT
13	250	-54	70	-41	255	23	LGHT
18	265	-56	62	-35	258	20	LGHT
22	275	-56	54	-29	261	17	LGHT
27	287	-56	48	-25	263	15	LGHT
28	289	-56	40	-20	264	14	LGHT
29	291	-58	32	-15	264	14	LGHT
31	295	-58	26	-11	265	13	LGHT
32	297	-58	18	-7	265	13	LGHT
32	297	-58	10	-2	265	12	LGHT
30	293	-60	2	2	264	14	LGHT
29	291	-60	-6	7	264	14	LGHT
27	287	-60	-14	12	263	15	LGHT
25	282	-60	-20	15	262	15	LGHT
24	280	-62	-28	20	260	18	LGHT
23	278	-62	-36	24	258	20	LGHT
23	278	-62	-44	29	256	22	LGHT
20	270	-62	-50	33	253	25	LGHT
16	259	-64	-58	38	246	31	LGHT
12	246	-64	-66	44	239	39	LGHT
9	235	-64	-72	48	229	49	LGHT
2	186	-64	-80				SKY
1	172	-66	-88				SKY

APPENDIX C

DETERMINATION OF AVERAGE TEMPERATURE

We wish to derive a relationship between the temperature at the center of a circular field of view and the temperature T_a that would be inferred from the flux average taken over the field. Consider a field of view defined by $x^2 + y^2 = 1$, with a temperature T_0 at the center and a linear temperature gradient across the field. Let ΔT be the temperature difference between the center and the edge along the x direction. If we take the flux to vary as T^n, we have for T_a:

$$T_a^n = \frac{\int_{-1}^{1} (T_0 + x\Delta T)^n \, 2y \, dx}{\int_{-1}^{1} 2y \, dx} \quad . \qquad \text{(C-1)}$$

If we write $y = \sqrt{1 - x^2}$ and make the substitution $\sin \xi \equiv x$, equation (C-1) becomes:

$$T_a^n = \frac{2}{\pi} \int_{-\pi/2}^{\pi/2} (T_0 + \Delta T \sin \xi)^n \cos^2 \xi \, d\xi \quad . \qquad \text{(C-2)}$$

I have solved this equation under the assumption that $\Delta T/T_0$ is small, so that terms of higher order than $(\Delta T/T_0)^2$ can be neglected:

$$T_a^n \cong T_0^n \left[1 + \frac{n(n-1)}{8} \left(\frac{\Delta T}{T_0} \right)^2 \right]$$

$$T_a \cong T_0 \left[1 + \frac{n-1}{8} \left(\frac{\Delta T}{T_0} \right)^2 \right] \quad . \tag{C-3}$$

The correct value for n can be found from the Planck function. For $\lambda T > 3$ cm deg, we can write for small changes in T:

$$n \simeq \frac{hc}{k\lambda T} = \frac{1.439}{\lambda T} \quad . \tag{C-4}$$

At $\lambda = 10\ \mu$, this approximation holds over the temperature range of interest, where n varies from 4.8 to 8.0 as T drops from 300 to 180°K.

An examination of Figure 5 in the text shows that $\Delta T/T$ is always less than 10%, so that the error in the temperature introduced by the instrumental averaging of flux is less than 1% and can therefore be neglected.

BIOGRAPHICAL NOTE

DAVID MORRISON received the B.A. degree from the University of Illinois in 1962 and the M.A. degree from Harvard University in 1964.

Mr. Morrison is currently a Ph. D. degree candidate at Harvard University holding a Smithsonian Graduate Research Fellowship. He has previously been employed at the Smithsonian Astrophysical Observatory, the Jet Propulsion Laboratory, and the Naval Research Laboratory.

Mr. Morrison's principal research interests are in planetary physics, especially the measurement and interpretation of microwave radio temperatures of the terrestrial planets.

NOTICE

This series of Special Reports was instituted under the supervision of Dr. F. L. Whipple, Director of the Astrophysical Observatory of the Smithsonian Institution, shortly after the launching of the first artificial earth satellite on October 4, 1957. Contributions come from the Staff of the Observatory.

First issued to ensure the immediate dissemination of data for satellite tracking, the reports have continued to provide a rapid distribution of catalogs of satellite observations, orbital information, and preliminary results of data analyses prior to formal publication in the appropriate journals. The Reports are also used extensively for the rapid publication of preliminary or special results in other fields of astrophysics.

The Reports are regularly distributed to all institutions participating in the U. S. space research program and to individual scientists who request them from the Publications Division, Distribution Section, Smithsonian Astrophysical Observatory, Cambridge, Massachusetts 02138.